Chapter 5

Nonlinear Results

THE EQUATIONS DEVELOPED in Chapters 2 and 3 provide a relatively simple yet accurate model of the dynamics underlying electrostatic tokamak turbulence. Using the flux-tube simulation geometry discussed in Chapter 4, we have developed high resolution nonlinear 3D toroidal simulations to investigate the nonlinear dynamics of tokamak turbulence via direct numerical simulations. Having demonstrated the efficacy of this flux-tube simulation geometry in Section 4.7, this Chapter investigates the nonlinear dynamics in more detail. These simulations have revealed several interesting features of toroidal microinstability driven turbulence, including the importance of nonlinear generation and damping of sheared $\mathbf{E} \times \mathbf{B}$ flows, a nonlinear peak in the fluctuation spectrum at much longer wavelengths than the fastest growing linear modes, similar to experimental measurements on TFTR [Fonck *et al.*, 1993] (also seen in full torus gyrokinetic particle simulations [Parker *et al.*, 1993]), and much larger heat fluxes and fluctuation levels than those observed in sheared slab simulations. Finally, using the bounce averaged trapped electron fluid equations, toroidal simulation results are presented which simultaneously retain the toroidal ITG drive and the TEM drive, allowing calculation of both ion and electron heat transport and particle transport.

5.1 Fluctuation Spectra

One of the most interesting features of these toroidal simulations is the long wavelength peak in the fluctuation spectra, consistent with BES measurements on TFTR

[FONCK *et al.*, 1993]. A contour plot of the linear growth rates vs. k_x and k_y is shown in Fig. 5.1 for the parameters: $\hat{s} = 1.5$, $q = 2$, $\eta_i = 4$, $\epsilon_n = 0.4$ and $T_i = T_e$, using the four moment toroidal gyrofluid equations with adiabatic electrons. These parameters are from TFTR L-mode shot #41309 at $r_0 = 53$cm, and are the same parameters used in the runs in Section 4.7. As described in Section 4.6, k_y corresponds to k_θ and k_x corresponds to θ_0 in the ballooning representation. There may be several eigenmodes for a given k_x and k_y corresponding to different mode structures along the field line. With the initial value toroidal gyrofluid code, the fastest growing of these eigenmodes eventually dominates, and it is this largest growth rate which is plotted in Fig. 5.1, in normalized units, $\gamma L_n/v_{ti}$. As discussed in Chapter 4, k_x corresponds to the radial wavevector (k_r) and k_y corresponds to the poloidal wavevector (k_θ). The anisotropy of the linear growth rate spectrum in k_x and k_y arises from "good" and "bad" curvature effects, as discussed in Section 1.3. At poloidal angle $\theta = \theta_0 = -k_x/k_y\hat{s}$, $k_\perp$ is minimized, and FLR stabilization tends to localize the mode near this poloidal angle through magnetic shear. If $\cos(\theta_0) > 0$, the modes are localized in the bad curvature region and are unstable, and modes with $\cos(\theta_0) < 0$ are localized in the good curvature region and are stable. The lines $k_x = \pm k_y\hat{s}\pi/2$, $k_x = \pm k_y\hat{s}3\pi/2$, etc., determine the boundary between modes localized in the good and bad curvature regions. The wedge of unstable modes with $-k_y\hat{s}\pi/2 < k_x < k_y\hat{s}\pi/2$ are localized in the bad curvature region $-\pi/2 < \theta < \pi/2$. There are also unstable wedges of modes with $-k_y\hat{s}5\pi/2 < k_x < -k_y\hat{s}3\pi/2$ and $k_y\hat{s}3\pi/2 < k_x < k_y\hat{s}5\pi/2$ localized in the bad curvature regions farther along the field line, at $-5\pi/2 < \theta < -3\pi/2$ and $3\pi/2 < \theta < 5\pi/2$. The linear growth rate spectrum peaks near $k_y\rho_i = 0.35$.

In the nonlinear simulations, these modes grow linearly until the $\mathbf{E}\times\mathbf{B}$ nonlinearities are no longer negligible compared to the linear terms. At the beginning of the nonlinear stage, the spectrum is dominated by the fastest growing modes. The $\mathbf{E}\times\mathbf{B}$ nonlinearities transfer energy between different $\mathbf{k}_\perp$ modes until a statistically steady but turbulent steady state is reached. The nonlinear fluctuation spectrum is obtained by averaging in time over this saturated steady state. Averaging over several different realizations (runs with different initial conditions) is theoretically more sound, but should be equivalent if the turbulence is stationary and the time averaging is over many correlation times (by the ergodic theorem). Fig. 5.2 shows contours of the energy spectrum in $\mathbf{k}_\perp$ space, $E(k_x, k_y) = \left\langle n^2 + u_\parallel^2 + T_\parallel^2/2 + T_\perp^2 \right\rangle/2$

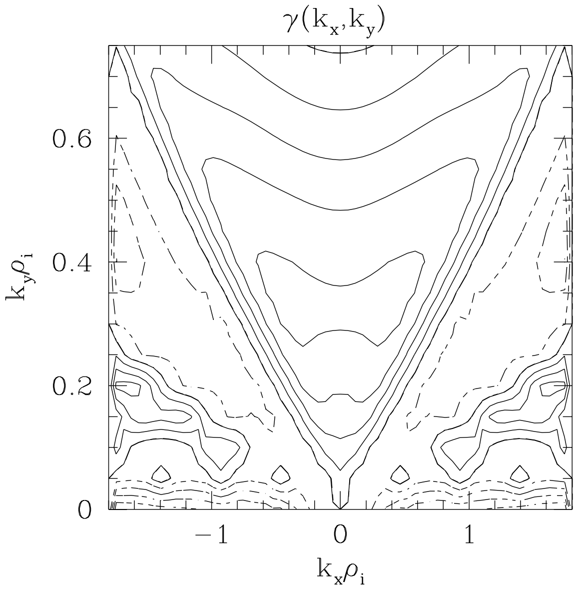

Figure 5.1: Linear growth rate spectrum for TFTR L-mode #41309 at $r_0 = 53$cm. The contours are at $\gamma = \pm 0,\ 0.05,\ 0.1,\ 0.15,\ 0.2\, v_{ti}/L_n$, with solid lines for $\gamma \geq 0$ and dashed for $\gamma < 0$. The peak growth rate is $\gamma \approx 0.2 v_{ti}/L_n$, at $k_\theta \rho_i \approx 0.35$.

(defined by Eq. (5.14) in the next section) averaged over the saturated state from $t = 75 - 170\, L_n/v_t$, for a run using the #41309 parameters above, using the four moment gyrofluid model and adiabatic electrons. The $\Phi^2(k_x, k_y)$ spectrum is very similar, as shown in Section 4.7. The nonlinear energy spectrum is concentrated at $k_\theta \rho_i \approx 0.15$. By comparison with Fig. 5.1, this is at significantly longer wavelength than the fastest growing linear modes. The nonlinear spectrum remains anisotropic in (k_x, k_y), but there is a tendency towards isotropy at high $\mathbf{k}_\perp$, compared to Fig. 5.1.

5.2 Nonlinear Energy Balance

To investigate the nonlinear dynamics, it is useful to construct a quadratic energy-like quantity for the fluctuations:

$$E = \frac{1}{2} \left\langle n^2 + u_\parallel^2 + T_\parallel^2/2 + T_\perp^2 \right\rangle, \tag{5.1}$$

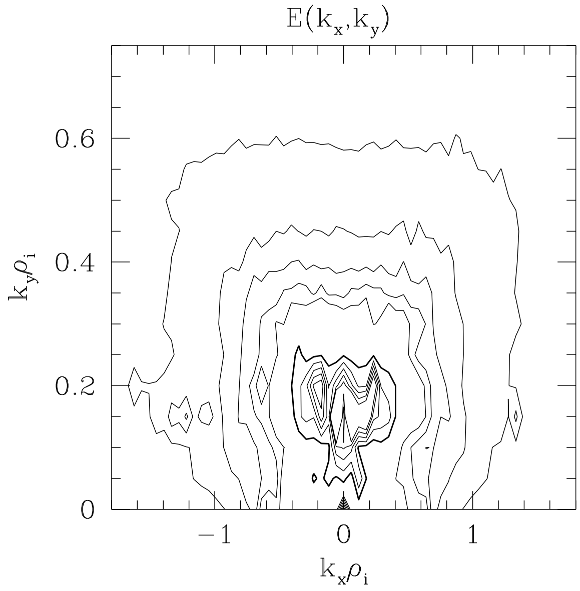

Figure 5.2: Time averaged nonlinear energy spectrum for #41309 parameters. Contours are at 0, 0.1, 0.2, 0.3, 0.4, 0.5, 1, 1.5, 2, 2.5, 3, and the $E = 1$ contour is bold for reference.

where $\langle\,\rangle$ is an average over the simulation volume:

$$\langle AB\rangle = \frac{1}{L_x L_y L_z}\int dx dy dz AB.$$

for any fluctuating quantities A and B. For simplicity, we will use the 3+1 model in Section 2.7 to find the evolution of this energy, neglecting collisions and the mirroring terms ($\epsilon = 0$). Some terms in Eqs. (2.102-2.105) vanish upon volume averaging due to the periodicity of the simulation domain: $\langle A\mathbf{v}_\Psi \cdot \nabla A\rangle = \langle A\hat{\hat{\nabla}}{}^2_\perp \mathbf{v}_\Psi \cdot \nabla A\rangle = 0$, leaving:

$$\begin{aligned}
\left\langle n\frac{\partial n}{\partial t}\right\rangle &= -\left\langle n[\frac{1}{2}\hat{\nabla}^2_\perp \mathbf{v}_\Psi]\cdot\nabla T_\perp\right\rangle - \langle n\nabla_\parallel u_\parallel\rangle + \left\langle n\left(1+\frac{\eta_\perp}{2}\hat{\nabla}^2_\perp\right) i\omega_* \Psi\right\rangle \qquad (5.2)\\
&\quad - \left\langle n\left(2+\frac{1}{2}\hat{\nabla}^2_\perp\right) i\omega_d\Psi\right\rangle - i\left\langle n\omega_d(p_\parallel + p_\perp)\right\rangle,\\
\left\langle u_\parallel\frac{\partial u_\parallel}{\partial t}\right\rangle &= -\langle u_\parallel\nabla_\parallel p_\parallel\rangle - \langle u_\parallel\nabla_\parallel\Psi\rangle - \langle u_\parallel 4i\omega_d u_\parallel\rangle - \langle u_\parallel 2|\omega_d|\nu_5 u_\parallel\rangle, \qquad (5.3)\\
\left\langle T_\parallel\frac{\partial T_\parallel}{\partial t}\right\rangle &= -\langle T_\parallel 2\nabla_\parallel u_\parallel\rangle - \left\langle T_\parallel\sqrt{2}\chi_\parallel|k_\parallel|T_\parallel\right\rangle + \langle T_\parallel\eta_\parallel i\omega_*\Psi\rangle - \langle T_\parallel 2i\omega_d\Psi\rangle \qquad (5.4)
\end{aligned}$$

$$
\begin{aligned}
& - \langle T_\parallel i\omega_d(6p_\parallel - 4n)\rangle - \langle T_\parallel 2|\omega_d|(\nu_1 T_\parallel + \nu_2 T_\perp)\rangle\,, \\
\left\langle T_\perp \frac{\partial T_\perp}{\partial t}\right\rangle \; = \; & - \left\langle T_\perp [\tfrac{1}{2}\hat{\nabla}_\perp^2 \mathbf{v}_\Psi]\cdot\nabla n\right\rangle - \left\langle T_\perp \sqrt{2}\chi_\perp |k_\parallel| \left(T_\perp + \frac{1}{2}\hat{\nabla}_\perp^2\Psi\right)\right\rangle \qquad (5.5) \\
& + \left\langle T_\perp \left[\frac{1}{2}\hat{\nabla}_\perp^2 - \eta_\perp(1+\hat{\hat{\nabla}}{}_\perp^2)\right] i\omega_*\Psi\right\rangle - \left\langle T_\perp\left(1+\hat{\nabla}_\perp^2+\hat{\hat{\nabla}}{}_\perp^2\right) i\omega_d\Psi\right\rangle \\
& - \langle T_\perp i\omega_d(4p_\perp - 3n)\rangle - \langle T_\perp 2|\omega_d|(\nu_3 T_\parallel + \nu_4 T_\perp)\rangle\,.
\end{aligned}
$$

Adding these together as in Eq. (5.1), some more terms cancel from periodicity: $\langle A\nabla_\parallel B\rangle = -\langle B\nabla_\parallel A\rangle$, $\langle A\omega_d B\rangle = -\langle B\omega_d A\rangle$, $\langle A\omega_* B\rangle = -\langle B\omega_* A\rangle$, and $\left\langle n[\frac{1}{2}\hat{\nabla}_\perp^2\mathbf{v}_\Psi]\cdot\nabla T_\perp\right\rangle = -\left\langle T_\perp[\frac{1}{2}\hat{\nabla}_\perp^2\mathbf{v}_\Psi]\cdot\nabla n\right\rangle$. For this definition of the fluctuation energy, Eq. (5.1), all the nonlinear FLR terms (cubic in perturbed quantities) cancel, so the final energy evolution contains only quadratic quantities and is given by:

$$
\frac{\partial E}{\partial t} = D_* + D_{dr} + D_\parallel + D_{di} + W_{u\Psi} = T. \qquad (5.6)
$$

The terms that affect the total energy evolution can be grouped into five classes: drive from the equilibrium gradients, D_*, reactive contributions from the real parts of the toroidal terms, D_{dr}, parallel Landau damping, $D_\parallel$, damping from toroidal phase mixing (from the imaginary parts of the toroidal terms), D_{di}, and parallel electric field work, $W_{u\Psi}$:

$$
\begin{aligned}
D_* \; &= \; \langle n(1+\frac{\eta_\perp}{2}\hat{\nabla}_\perp^2)i\omega_*\Psi\rangle + \frac{\eta_\parallel}{2}\langle T_\parallel i\omega_*\Psi\rangle \qquad (5.7) \\
& \quad + \langle T_\perp[\frac{1}{2}\hat{\nabla}_\perp^2 + \eta_\perp(1+\hat{\hat{\nabla}}{}_\perp^2)]i\omega_*\Psi\rangle, \\
D_{dr} \; &= \; -\langle n(2+\frac{1}{2}\hat{\nabla}_\perp^2)i\omega_d\Psi\rangle - \langle T_\parallel i\omega_d\Psi\rangle - \nu_{2i}\langle T_\parallel i\omega_d T_\perp\rangle \qquad (5.8) \\
& \quad -\nu_{3i}\langle T_\perp i\omega_d T_\parallel\rangle - \langle T_\perp(1+\hat{\nabla}_\perp^2+\hat{\hat{\nabla}}{}_\perp^2)i\omega_d\Psi\rangle, \\
D_\parallel \; &= \; \frac{\sqrt{2}}{2}\chi_\parallel\langle T_\parallel|k_\parallel|T_\parallel\rangle + \sqrt{2}\chi_\perp\langle T_\perp|k_\parallel|(T_\perp+\frac{1}{2}\hat{\nabla}_\perp^2\Psi)\rangle, \qquad (5.9) \\
D_{di} \; &= \; -2\nu_{5r}\langle u_\parallel|\omega_d|u_\parallel\rangle - \nu_{1r}\langle T_\parallel|\omega_d|T_\parallel\rangle - \nu_{2r}\langle T_\parallel|\omega_d|T_\perp\rangle \qquad (5.10) \\
& \quad -2\nu_{3r}\langle T_\perp|\omega_d|T_\parallel\rangle - 2\nu_{4r}\langle T_\perp|\omega_d|T_\perp\rangle\,, \\
W_{u\Psi} \; &= \; -\langle u_\parallel\nabla_\parallel\Psi\rangle. \qquad (5.11)
\end{aligned}
$$

As a test of the numerical accuracy of the nonlinear simulations, we evaluate these driving and damping terms and compare them to the actual time evolution of the energy. The degree to which the simulations reproduce these conservation

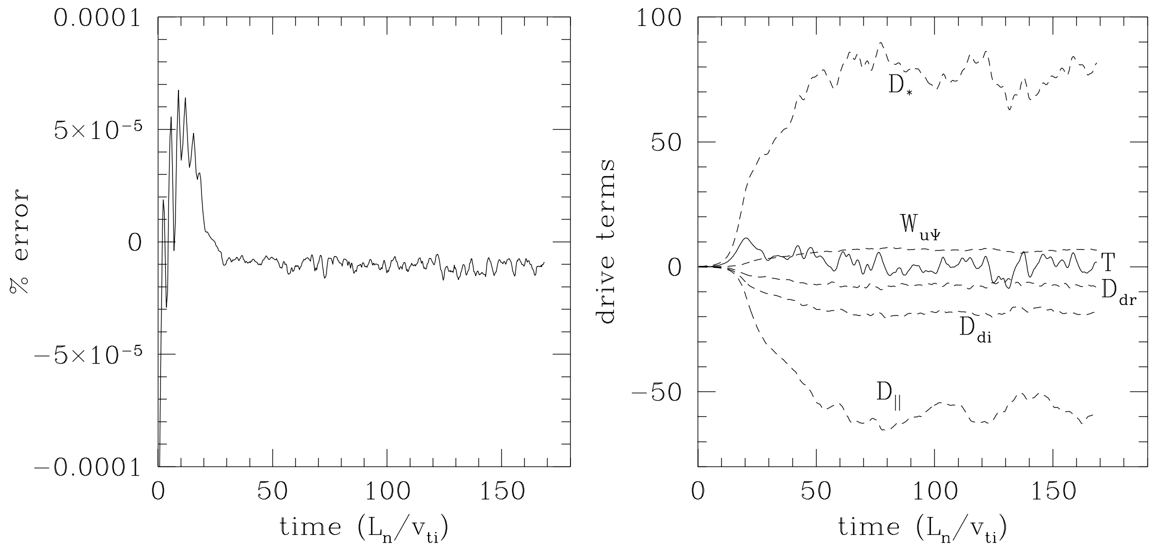

Figure 5.3: Energy conservation and time evolution of the various drive terms for a nonlinear run at the #41309 parameters.

properties of the equations is shown in Fig. 5.3 by plotting:

$$\%\,\mathrm{error} = \frac{\partial E/\partial t - T}{E}. \tag{5.12}$$

The energy balance Eq. (5.6) is preserved quite well.

At saturation, where $E \approx$ constant, it is interesting to look at the relative nonlinear magnitudes of the five driving and damping terms in Eq. (5.6). The time evolution of these terms for the #41309 run is shown in Fig. 5.3. For these parameters, the dominant drive is from equilibrium gradients, not from toroidal terms. This is to be expected because ω_d is not by itself a free energy source for instabilities. The local dispersion relation involves (see Eq. (2.56)):

$$g = F_0 \frac{\omega - \omega_*^T}{\omega - k_\parallel v_\parallel - \omega_{dv}} J_0 \frac{e\Phi}{T_0}, \tag{5.13}$$

where ω_*^T drives instabilities, but ω_d only appears in the resonant denominator. The dominant damping in the nonlinear simulations is from parallel Landau damping, not from toroidal phase mixing, although the amount by which parallel damping dominates can depend on the physical parameters of the run.

Because the toroidal gyrofluid equations constitute a multiple field system with many nonlinearities, constructing a simple nonlinear transfer function is more difficult than, for example, in the Hasegawa-Mima equation [HASEGAWA and MIMA, 1977]. Nevertheless, we can begin to investigate the nonlinear dynamics by looking at the energy spectrum in k_x and k_y, obtained by averaging only over the parallel direction:

$$E(k_x, k_y) = \frac{1}{L_z} \int dz \frac{1}{2} \left(n^2 + u_\parallel^2 + \frac{1}{2} T_\parallel^2 + T_\perp^2 \right). \tag{5.14}$$

Similarly, $\mathbf{k}_\perp$ dependent drive terms can be defined by integrating only over z:

$$T(k_x, k_y) = D_*(k_x, k_y) + D_{dr}(k_x, k_y) + \cdots, \tag{5.15}$$

where D_*, D_{dr}, etc., are as given in Eqs. (5.7-5.11), but with $\langle\,\rangle$ now representing only integration over z, with a few additional terms which are not cancelled by integration over y. The evolution of the $\mathbf{k}_\perp$ dependent energy is now given by:

$$\frac{\partial}{\partial t} E(k_x, k_y) = T(k_x, k_y) + N(k_x, k_y), \tag{5.16}$$

where $N(k_x, k_y)$ represents energy transfer from the nonlinear terms (triple correlation terms in the $E(\mathbf{k}_\perp)$ energy balance). Note that at saturation, $\int dxdy\, T(x, y) \propto \sum_{k_x,k_y} T(k_x, k_y) = 0$ and $\sum_{k_x,k_y} N(k_x, k_y) = 0$. The total drive, $T(k_x, k_y)$ shows where the energy is coming in linearly in $\mathbf{k}_\perp$ space. The nonlinear terms convect energy around in $\mathbf{k}_\perp$ space to provide the balance $\partial E(k_x, k_y)/\partial t = 0$ for each $\mathbf{k}_\perp$ at saturation. The total drive is plotted in Fig. 5.4 for the #41309 run. The most interesting feature of this plot is that the linear drive is coming in where the spectrum peaks, at long wavelengths, and not at the shorter wavelengths where the linear growth rate is larger. This implies that at saturation, there is not a strong nonlinear transfer of energy from modes with the largest linear growth rates to the energy containing modes. Most of the nonlinear energy transfer in $\mathbf{k}_\perp$-space is from the energy containing range to longer wavelengths which are damped. However, since $T(k_x, k_y)$ is averaged in z, it *only* diagnoses the energy transfer in $\mathbf{k}_\perp$-space. The dominant energy transfer could very well be from low $k_\parallel$ to high $k_\parallel$, since parallel Landau damping is dominant. More detailed diagnostics are required to isolate and identify these various possible cascade mechanisms. We can also construct a nonlinear growth rate, $T(k_x, k_y)/E(k_x, k_y)$ which is also plotted in Fig. 5.4.

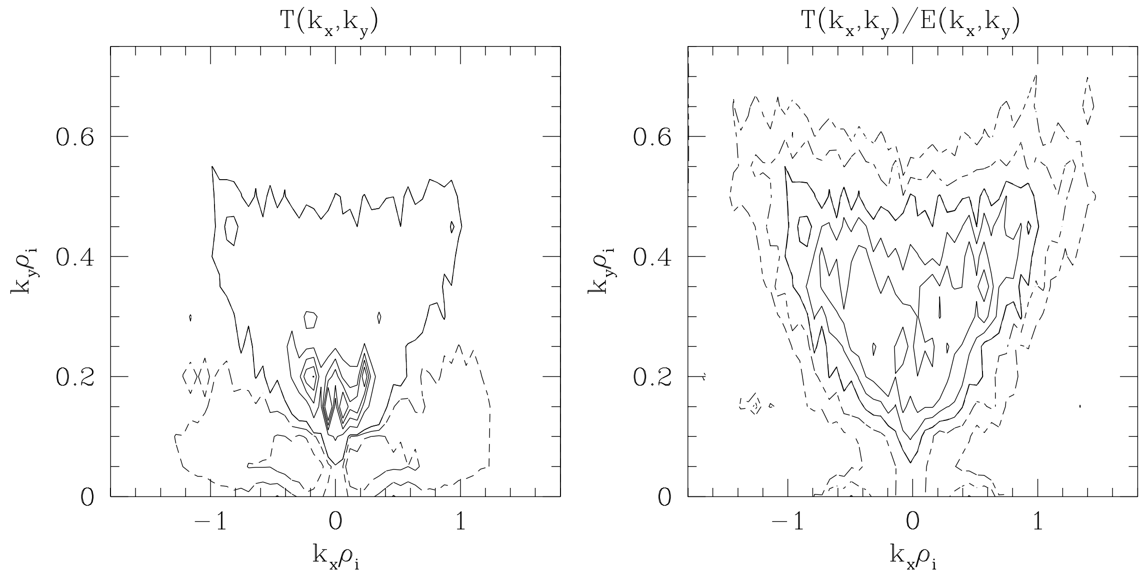

Figure 5.4: Time averaged total linear drive spectrum $T(k_x, k_y)$, and $T/E(k_x, k_y)$ spectrum, for the #41309 run. Contours for T are at -0.1, -0.05, 0, 0.25, 0.5, 0.75, 1, and contours for T/E are at -0.2, -0.1, 0, 0.1, 0.2.

Clearly, much more work is need to understand the nonlinear dynamics in more detail, beyond these cursory investigations. It is of great interest to understand the processes which set the dominant nonlinear scale.

5.3 Nonlinear Generation and Damping of Sheared $\mathbf{E} \times \mathbf{B}$ Flows

Both slab [Dorland *et al.*, 1992; Dorland, 1993] and toroidal [Beer *et al.*, 1992; Hammett *et al.*, 1993] simulations have revealed that an important nonlinear saturation process for core tokamak turbulence is the nonlinear generation and damping of sheared $\mathbf{E} \times \mathbf{B}$ flows. The amplitude of these flows is determined by the balance between the nonlinear generation and linear damping of the poloidal component of these flows. The amplitude of these flows is a sensitive control of the turbulence levels and transport. In this section the effects of these flows are discussed, and the gyrofluid models of the linear damping processes are carefully investigated.

It should be emphasized that in these simulations, the sheared $\mathbf{E} \times \mathbf{B}$ flows are small-scale flows generated by the turbulence, with $k_r \rho_i \sim 0.1$, and evolve on the turbulent time scales. This is in contrast to most theoretical and experimental studies of the shear flow stabilization, where the effects of large scale $\mathbf{E} \times \mathbf{B}$ flows are considered, with $k_r L_n \sim \mathcal{O}(1)$. The large scale flows evolve on the slower transport time scale, except right at the L-H transition, and are equilibrium flows within the gyrokinetic ordering. We have not considered the effects of *equilibrium* sheared $\mathbf{E} \times \mathbf{B}$ flows or sheared parallel flows on our simulations, although these effects can be incorporated.

5.3.1 Proper Treatment of Adiabatic Electron Response

When the electrons are assumed to be adiabatic (or are nearly adiabatic) it is important to use an expression for the perturbed electron density that allows consistent evolution of sheared $\mathbf{E} \times \mathbf{B}$ flows. A historical review of various assumptions about the adiabatic electron response is given in [Dorland, 1993]. Adiabatic electrons experience no net radial transport since the $\mathbf{E} \times \mathbf{B}$ convection of the perturbed electron density is zero ($\mathbf{E} \times \mathbf{B} \cdot \nabla \tilde{n}_e \propto \nabla \tilde{\Phi} \times \mathbf{B} \cdot \nabla \tilde{\Phi} = 0$). If the electrons are allowed to respond to a potential perturbation which is constant on a flux surface, this implies net radial transport of electrons, which is unphysical unless the magnetic field is stochastic. Thus for adiabatic electrons, it is essential to use [Dorland and Hammett, 1993]:

$$n_e = \tau \left(\Phi - \langle \Phi \rangle \right), \tag{5.17}$$

where $\tau = T_{i0}/T_{e0}$, Φ has been normalized to e/T_{i0}, and $\langle \Phi \rangle$ is a flux surface average.

The effect of this proper adiabatic response on our toroidal nonlinear simulations is shown in Fig. 5.5. These simulations used the six moment toroidal gyrofluid equations and assumed adiabatic electrons. The parameters correspond to TFTR L-mode shot #65018 at $r/a = 0.78$: $\epsilon = 0.25$, $\epsilon_n = 0.26$, $\eta_i = 2.31$, $\hat{s} = 1.7$, $q = 3.42$, and $T_i/T_e = 1.19$. Because this is near the edge, $\hat{s}$ is relatively large. When $n_e = e\Phi/T_e$ is used, radially elongated structures form and grow, showing no signs of saturating throughout the length of this run. When the $k_\theta = 0$, $k_\parallel = 0$ components of Φ are artificially suppressed, so $\langle \Phi \rangle = 0$, there is no $\mathbf{E} \times \mathbf{B}$ rotation. It is curious that the simulations with $n_e = \tau\Phi$ behave so differently from the those with $\langle \Phi \rangle = 0$. Using $n_e = \tau(\Phi - \langle \Phi \rangle)$ allows nonlinear generation of radially sheared

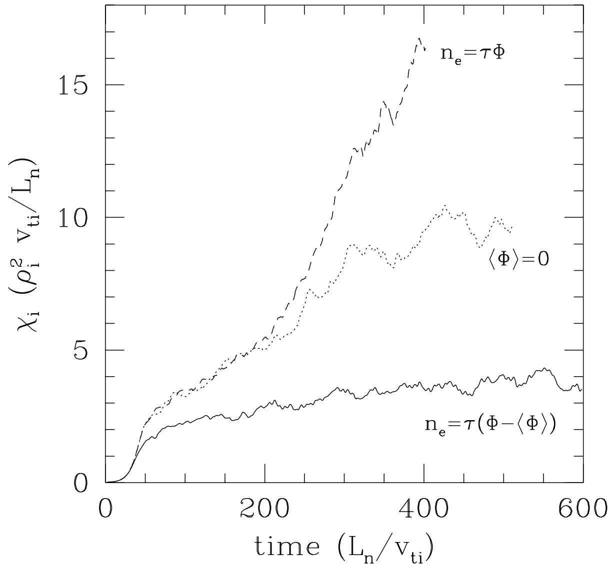

Figure 5.5: Effect of the proper adiabatic response in nonlinear simulations. When $n_e = e\Phi/T_e$ is used (dashed line), radially elongated structures form and grow throughout the run. Using $n_e = e(\Phi - \langle\Phi\rangle)/T_e$ allows nonlinear generation of radially sheared $\mathbf{E}\times\mathbf{B}$ flows, which rip apart these radially elongated structures (solid line). A saturated state is reached where the turbulence generated sheared $\mathbf{E}\times\mathbf{B}$ flows in turn regulate the turbulence. Also shown (dotted line) is a run forcing the flux surface averaged Φ to zero, disallowing sheared flows.

$\mathbf{E}\times\mathbf{B}$ flows, which rip apart these radially elongated structures. A saturated state is reached where the turbulence generated sheared $\mathbf{E}\times\mathbf{B}$ flows in turn regulate the turbulence. This interplay leads to lower fluctuation and turbulence levels than the case with no sheared $\mathbf{E}\times\mathbf{B}$ flows.

It is interesting to investigate why the adiabatic response $n_e = \tau\left(\Phi - \langle\Phi\rangle\right)$, as opposed to $n_e = \tau\Phi$, has such a dramatic effect on the nonlinear evolution. Consider a potential perturbation as shown in Fig. 5.6, which is constant on a flux surface, i.e. $k_\theta = k_\parallel = 0$, but is radially varying. In this figure, r is a small fraction of the minor radius of the tokamak. Since this perturbation has $k_\parallel = 0$, if $n_e = \tau\Phi$ were used for the adiabatic electron response, the flux surface averaged perturbed electron density, $n_e(r)$, would have radial variation, as shown below $\Phi(r)$. The perturbation on the left of Fig. 5.6 could evolve into the perturbation on the right, and this would

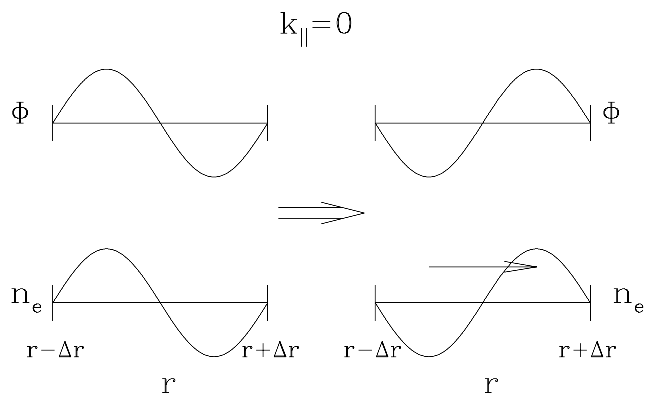

Figure 5.6: A possible evolution of the electrostatic potential, showing the necessity of the form Eq. (5.17) for the adiabatic response. The potential perturbation on the left could evolve into the perturbation on the right, implying nonphysical net radial transport of adiabatic electrons if $n_e/n_{e0} = e\Phi/T_e$. If $n_e/n_{e0} = e(\Phi - \langle\Phi\rangle)/T_e$, the electrons do not respond to the flux surface averaged component.

imply a net radial transport of electrons, which is unphysical if the electrons are adiabatic. Thus, the electrons should not respond to the $k_\theta = k_\parallel = 0$ component of the potential, leading to Eq. (5.17). The electrons *can* respond to potential perturbations with $k_\parallel \neq 0$, since in this case the flux surface averaged perturbed electron density is zero and there is no net radial electron transport. The form Eq. (5.17) is essential to properly describe the evolution of radially varying potential perturbations, which gives rise to sheared perpendicular $\mathbf{E} \times \mathbf{B}$ flow. Assuming $n_e = \tau\Phi$ essentially allows the electrons to move radially, so they effectively short out these components of the potential. Using Eq. (5.17) prohibits radial motion of adiabatic electrons, and allows the self-consistent generation of sheared $\mathbf{E} \times \mathbf{B}$ flows.

The turbulence level is very sensitive to the damping of these flux surface averaged $\mathbf{E} \times \mathbf{B}$ flows, as shown in Fig. 5.7 The damping of the $k_\theta = 0$ modes is dominantly due to the toroidal effects associated with magnetic pumping which damp the (large) poloidal component of this flow. These effects are independent of k_r for small $k_r\rho_i$, and dominate over viscous effects which are proportional to $\nu_{ii}\nabla_\perp^2$. The poloidal damping can be turned off in the simulations by artificially setting

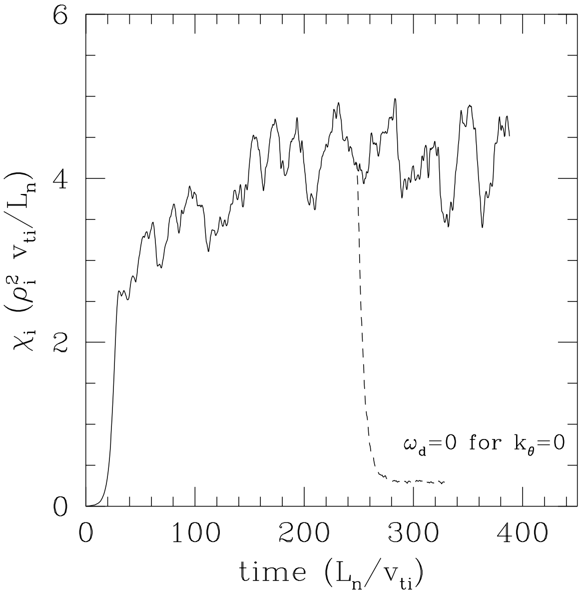

Figure 5.7: Effect of poloidal flow damping on the nonlinear saturation level. At $t = 250L_n/v_t$, the poloidal flow damping is artificially turned off by setting $\omega_d = 0$ for $k_\theta = 0$ modes (dashed line). Compared to the case *with* flow damping (solid line), the $\mathbf{E} \times \mathbf{B}$ flows grow to much larger amplitude and greatly reduce the fluctuation levels and transport.

$\omega_d = 0$ for these modes, which for $k_\theta = 0$ is normally $\omega_d = -k_r \epsilon_n \sin(\theta)$. Fig. 5.7 shows a simulation with the proper treatment which was restarted at $t = 250L_n/v_{ti}$ with $\omega_d = 0$ for the $k_\theta = 0$ rotation modes. This allows the sheared rotation to grow to much larger amplitude, and the turbulence level is greatly reduced.

The radial variation of the flux surface averaged potential $\langle\Phi\rangle$ and parallel flow $\langle u_\parallel\rangle$ are shown in Fig. 5.8, plotted at the end ($t = 170L_n/v_{ti}$) of the simulation discussed in Sections 5.1 and 5.2, i.e. for TFTR L-mode shot #41309 at $r/a =$ 53cm. Both radially sheared $\mathbf{E} \times \mathbf{B}$ flow and sheared parallel flow can enhance the radial decorrelation of the turbulence, reducing the fluctuation levels [Biglari *et al.*, 1990; Hahm, 1994]. (Large equilibrium sheared flows can also introduce a Kelvin-Helmholtz type instability, see for example [Waltz *et al.*, 1994a].) It is interesting to compare the relative strength of the radial decorrelation from the perpendicular $\mathbf{E} \times \mathbf{B}$ and the parallel flows. This is measured by the perpendicular and parallel shearing rates: $\omega_s^\perp = \Delta r\,\partial(k_\theta v_{E\theta})/\partial r$ and $\omega_s^\parallel = \Delta r\,\partial(k_\parallel u_\parallel)/\partial r$, where Δr is the radial correlation length of the turbulence (a typical eddy or blob size). Using a perpendicular correlation length $r_0\Delta\theta \approx 1/k_\theta$, the shearing rate from $v_E = ik_r\rho_i v_{ti}(e\Phi_1/T_{i0})$ is:

$$\omega_s^\perp \sim \Delta r \frac{\partial}{\partial r}\left(\frac{k_r\rho_i^2\Phi}{r_0\Delta\theta}\right)\frac{v_{ti}}{L_n}.$$

Recall that $e\Phi_1/T_{i0} = \Phi(\rho_i/L_n)$ and $u_1/v_{ti} = u_\parallel(\rho_i/L_n)$ in our normalization, Eq. 2.39. The shearing rate from parallel flow, since $k_\parallel \sim 1/qR$, see Figs. 4.12(b) and 4.13(b), is:

$$\omega_s^\parallel \sim \Delta r \frac{\partial}{\partial r}\left(\frac{\rho_i u_\parallel}{qR}\right)\frac{v_{ti}}{L_n}.$$

The shearing rate from perpendicular $\mathbf{E}\times\mathbf{B}$ flow is larger than that from parallel flow by

$$\frac{\omega_s^\perp}{\omega_s^\parallel} \sim \frac{k_r\rho_i^2\Phi}{r_0\Delta\theta}\frac{qR}{\rho_i u_\parallel} \sim (k_r\rho_i)(k_\theta\rho_i)\frac{qR}{\rho_i} \sim \frac{1}{\varepsilon},$$

in the gyrokinetic ordering. Using $\Phi \approx 5u_\parallel$ from Fig. 5.8, $k_r\rho_i \approx 0.15$ and $k_\theta\rho_i \approx \rho_i/(r_0\Delta\theta) \approx 0.15$ from the simulations, and the measured $q = 2.4$, $\rho_i = 0.14$cm, and $R = 258$cm yields $\omega_s^\perp \approx 500\,\omega_s^\parallel$, indicating that perpendicular flow shearing dominates over parallel flow shearing for the elongated turbulence ($k_\parallel \ll k_\perp$) in these toroidal simulations. Note that this is true for the flows generated by the turbulence, but does not preclude the importance of large scale equilibrium toroidal (mostly parallel) flows. In addition, since the radial scale of the flows and the turbulence are comparable, the parameters above lead to an estimate of the perpendicular shearing rate, $\omega_s^\perp \approx 0.2v_t/L_n$. The measured turbulent decorrelation time from the simulation is $\tau_c \sim 5L_n/v_{ti}$ (which can also be roughly estimated from the time scale of the fluctuations in the time history plots in Figs. 4.12(a) and 5.3). This leads to an estimate for the turbulent scattering rate of $\omega_T \sim 0.2v_{ti}/L_n$. The sheared flows should strongly influence the turbulence if $\omega_s \gtrsim \omega_T$, which is satisfied here. While these are rough estimates, it is clear that the levels of sheared $\mathbf{E}\times\mathbf{B}$ flow in the simulations is large enough to have a significant impact on the turbulence. Thus the conventional theoretical picture of the stabilizing influence of sheared $\mathbf{E}\times\mathbf{B}$ flow [Biglari *et al.*, 1990] on the turbulence seems consistent with the large effects observed in these simulations.

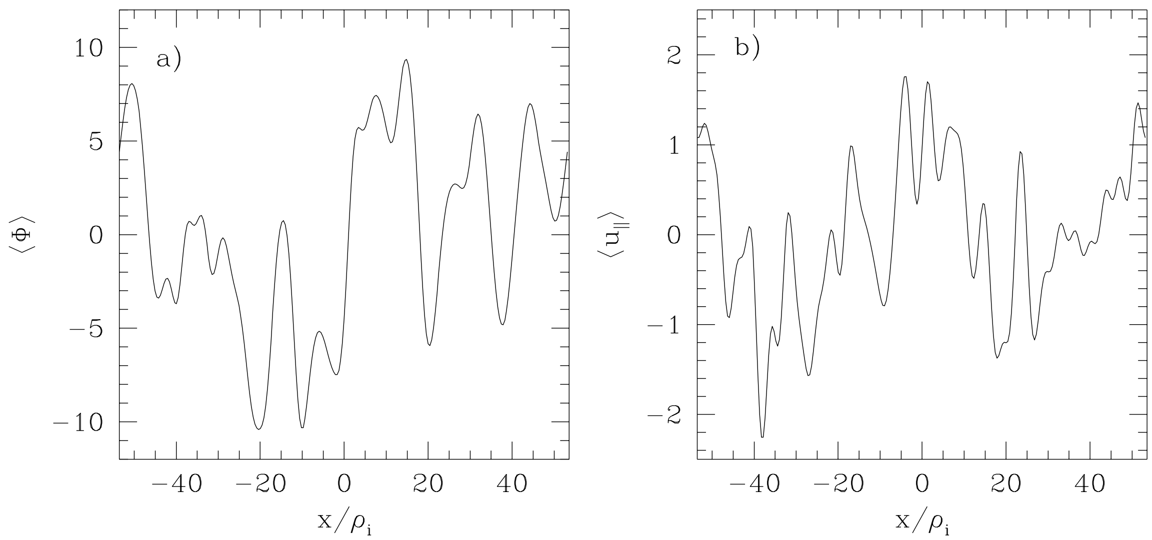

Figure 5.8: Flux surface averaged potential and parallel flow at the end of the simulation at the #41309 parameters. The radial variation (first derivative) of the potential leads to a perpendicular (mostly poloidal) $\mathbf{E} \times \mathbf{B}$ flow, which is radially sheared (second derivative of Φ).

5.3.2 Neoclassical Damping of Poloidal Flows

These sheared $\mathbf{E} \times \mathbf{B}$ flows are damped primarily by toroidal effects. While (classical) collisional damping would damp these flows in sheared slab geometry, in a toroidal system the strongest damping mechanism is neoclassical magnetic pumping. Magnetic pumping damps the (large) poloidal component of the $\mathbf{E} \times \mathbf{B}$ flow until the total flow (parallel flow plus $\mathbf{E} \times \mathbf{B}$ flow) is purely toroidal. Because this process arises from the variation of B with major radius, we have termed these effects "neoclassical," even though for turbulent time scales collisionless "transit-time magnetic pumping" [Stix, 1973] dominates over collisional effects. This damping arises from collisionless phase mixing (Landau damping), which dominates for short time scales, $t < \omega_{bi}^{-1}$, and damps the flows at a rate proportional to ω_{ti}. For these short times, $t < \omega_{bi}^{-1}$, trapped particles do not know that they are trapped, so the plateau regime damping rates are applicable. After a bounce time the Landau damping ceases because of trapping, and one then gets a slow decay due only to collisions. This collisionless transit-time magnetic pumping can also be related to the radial drifts of particle orbits in a tokamak in response to a changing radial electric field, i.e. a kind of neoclassical enhancement of the polarization drift [Stix, 1973; Hinton and Robertson, 1984; Callen, 1973].

In this section damping rates for magnetic pumping are derived from the toroidal gyrofluid equations derived in Chapter 2. It is shown that in the banana and plateau regimes the toroidal gyrofluid equations accurately capture transit-time magnetic pumping. The damping rate in the Pfirsch-Schlüter is also shown to agree with neoclassical theory, for completeness.

As discussed in Section 5.3.1, the most important flows are those with radial scales on the order of the turbulence scale size or longer. We see $k_r \rho_i \approx 0.1 - 0.2$ in our nonlinear simulations, so we will concentrate on the limit $k_r \rho_i \ll 1$, where magnetic pumping dominates over collisional viscous damping. Let us consider the dynamics of a potential perturbation which is constant of a flux surface, $\Phi = \Phi(r)$. The discussion closely follows [Hassam and Kulsrud, 1978], but extends their approach into collisionless regimes. The radially varying potential leads to a perpendicular $\mathbf{E} \times \mathbf{B}$ flow, $\mathbf{v}_E = (c/B)\hat{\mathbf{b}} \times \nabla\Phi$. Restricting the discussion to circular concentric flux surface geometry for simplicity, we have: $\hat{\mathbf{b}} = b_z[\mathbf{e}_\phi + (\epsilon/q)\mathbf{e}_\theta]$, $\epsilon = r/R_0$, $b_z^{-1} = \sqrt{1 + \epsilon^2/q^2}$, $\mathbf{e}_\phi$ is the toroidal direction, and $\mathbf{e}_\theta$ is the poloidal direction. The magnetic field strength is $B = B_0 R_0/R$, where B_0 is the field on axis, at $R = R_0$. In addition to the perpendicular flow, there may be a parallel flow $u_\parallel(r,\theta)$. In the small k_r limit which we consider here, $\Phi \gg p$, so the diamagnetic flow contribution is negligible. Both the perpendicular $\mathbf{E}\times\mathbf{B}$ flow and parallel flow have toroidal and poloidal components:

$$\mathbf{v}_E = \frac{c}{B}\frac{\partial\Phi}{\partial r} b_z \left(\mathbf{e}_\theta - \frac{\epsilon}{q}\mathbf{e}_\phi\right), \tag{5.18}$$

$$u_\parallel \hat{\mathbf{b}} = u_\parallel b_z \left(\mathbf{e}_\phi + \frac{\epsilon}{q}\mathbf{e}_\theta\right). \tag{5.19}$$

The toroidal and poloidal components of the total flow $\mathbf{v} = u_\parallel\hat{\mathbf{b}} + \mathbf{v}_E = v_\theta \mathbf{e}_\theta + v_\phi \mathbf{e}_\phi$ are:

$$v_\phi = (u_\parallel - \frac{\epsilon}{q}\frac{c}{B}\frac{\partial\Phi}{\partial r})b_z, \tag{5.20}$$

$$v_\theta = (u_\parallel \frac{\epsilon}{q} + \frac{c}{B}\frac{\partial\Phi}{\partial r})b_z. \tag{5.21}$$

Let us consider the time evolution of these flows, as described by the 4+2 toroidal gyrofluid equations, given in Section 2.6. The quasineutrality constraint for adiabatic electrons, Eq. (2.9), is $\tau(\Phi - \langle\Phi\rangle) = \bar{n}_i + (\Gamma_0 - 1)\Phi$, where Φ is normalized to e/T_i, $\bar{n}_i$ to n_{i0}, and $\tau = T_i/T_e$. It is convenient to introduce the notation $h = R/R_0 = 1 + \epsilon\cos\theta$, so the flux surface average is $\langle\Phi\rangle = (2\pi)^{-1}\oint d\theta h \Phi(r) = \Phi$. For $k_r\rho_i \ll 1$, $\bar{n}_i = n$ and $\Gamma_0 = 1 - k_r^2\rho_i^2$, so:

$$\langle\Phi\rangle = \frac{\langle n\rangle}{\langle k_r^2 \rho_i^2\rangle}. \tag{5.22}$$

We now normalize k_r to ρ_{i0}, where $\rho_{i0} = v_{ti} mc/eB_0$, so $\rho_i = \rho_{i0} h$ and $\langle\Phi\rangle = \langle n\rangle / k_r^2 \langle h^2\rangle$. Since we have assumed circular concentric surfaces, k_r is independent of θ. Now consider the evolution of the flux surface averaged toroidal angular momentum, $\langle h v_\phi\rangle$. Using Eq. (5.20),

$$\frac{\partial}{\partial t}\langle h v_\phi\rangle = \frac{\partial}{\partial t}\langle h u_\parallel b_z\rangle - \frac{\partial}{\partial t}\left\langle h \frac{\epsilon}{q}\frac{c}{B}\frac{\partial\Phi}{\partial r} b_z\right\rangle, \tag{5.23}$$

In the normalized units of Chapter 2 and Eq. (5.22), this becomes:

$$\frac{\partial}{\partial t}\langle h v_\phi\rangle = b_z \frac{\partial}{\partial t}\langle h u_\parallel\rangle - i\frac{b_z \epsilon}{q k_r}\frac{\partial\langle n\rangle}{\partial t}, \tag{5.24}$$

so we need to find $\partial \langle hu_\parallel \rangle / \partial t$ and $\partial \langle n \rangle / \partial t$ from the gyrofluid equations.

Considering perturbations with $k_y = 0$, so $\omega_* = 0$, but with slow parallel variation so $\partial/\partial\theta \neq 0$ (the y coordinate is perpendicular and θ is the parallel coordinate, as discussed in Chapter 4), the density and parallel velocity equations, Eqs. (2.91) and (2.92) become:

$$\frac{\partial n}{\partial t} + B\nabla_\parallel \frac{u_\parallel}{B} + 2i\omega_d \Phi + i\omega_d(p_\parallel + p_\perp) = 0, \tag{5.25}$$

$$\frac{\partial u_\parallel}{\partial t} + B\nabla_\parallel \frac{p_\parallel}{B} + \nabla_\parallel \Phi + p_\perp \nabla_\parallel \ln B + i\omega_d(q_\parallel + q_\perp + 4u_\parallel) = 0. \tag{5.26}$$

The parallel derivatives, $\nabla_\parallel = \hat{\mathbf{b}} \cdot \nabla = (b_z/qR_0)\partial/\partial\theta$, when normalized, become $\nabla_\parallel = (b_z\epsilon_n/q)\partial/\partial\theta$, where $\epsilon_n = L_n/R_0$. Furthermore, in these variables, $i\omega_d = (cT/eB^3)\mathbf{B} \times \nabla B \cdot \nabla = -ik_r b_z \epsilon_n \sin\theta$, and $\nabla_\parallel \ln B = (\epsilon_n \epsilon b_z/hq)\sin\theta$. Flux surface averaging the density equation yields:

$$\frac{\partial \langle n \rangle}{\partial t} = -\frac{1}{2\pi}\int d\theta h \left[\frac{b_z\epsilon_n}{q}\frac{B_0}{h}\frac{\partial}{\partial\theta}\frac{u_\parallel}{B} - ik_r b_z \epsilon_n \sin\theta(2\Phi + p_\parallel + p_\perp)\right]. \tag{5.27}$$

The $u_\parallel$ term vanishes on flux surface averaging, leaving:

$$\frac{\partial \langle n \rangle}{\partial t} = \frac{ik_r b_z \epsilon_n}{2\pi}\int d\theta \sin\theta(2\Phi + p_\parallel + p_\perp). \tag{5.28}$$

Averaging the parallel velocity equation leads to:

$$\frac{\partial}{\partial t}\langle hu_\parallel \rangle = -\frac{1}{2\pi}\int d\theta h^2 \frac{b_z\epsilon_n}{q}\left[\frac{\partial}{\partial\theta}(p_\parallel + \Phi) + \frac{\epsilon}{h}(p_\parallel - p_\perp) - ik_r q \sin\theta(q_\parallel + q_\perp + 4u_\parallel)\right]. \tag{5.29}$$

Using the identity:

$$\int d\theta h^2 \frac{\partial}{\partial\theta}(p_\parallel + \Phi) = 2\int d\theta h\epsilon \sin\theta(p_\parallel + \Phi), \tag{5.30}$$

Eqs. (5.28) and (5.29) can be combined. The k_r independent terms cancel, and:

$$\frac{\partial}{\partial t}\langle hv_\phi \rangle = \frac{ik_r b_z \epsilon_n}{2\pi}\int d\theta h^2 \sin\theta(q_\parallel + q_\perp + 4u_\parallel) \approx 0, \tag{5.31}$$

since we are considering the $k_r\rho_i \to 0$ limit.

Similarly, we can find the time evolution of the flux surface averaged parallel flow, $\langle u_\parallel/h \rangle \propto \langle \mathbf{v} \cdot \mathbf{B} \rangle$, which to zeroth order in k_r is given by:

$$\frac{\partial}{\partial t}\left\langle \frac{u_\parallel}{h} \right\rangle \approx \frac{1}{2\pi}\int d\theta \frac{b_z \epsilon_n \epsilon \sin\theta}{qh}(p_\parallel - p_\perp). \tag{5.32}$$

The parallel flow is damped by the difference between $p_\parallel$ and $p_\perp$. In neoclassical parlance, this expresses the fact that the parallel flow is damped by the parallel viscous stress $\mathbf{B} \cdot \nabla \cdot \boldsymbol{\pi}$ [Hirshman, 1978], where the stress tensor has the CGL form $\boldsymbol{\pi} = (p_\parallel - p_\perp)(\hat{\mathbf{b}}\hat{\mathbf{b}} - \mathbf{I}/3)$ [Chew *et al.*, 1956]. Keep in mind that the density and velocity gyrofluid equations are exact moments of the gyrokinetic equation in this limit (small $k_\perp$), so these equations for the toroidal and parallel flows are capturing the true physics. (In the six moment model closures are not introduced until the $p_\parallel$ and $p_\perp$ equations.)

The evolution of $\delta p = p_\parallel - p_\perp$ is found by subtracting the parallel and perpendicular pressure equations, Eqs. (2.93) and (2.94). Because $k_r \ll 1$, but $\Phi \sim n/k_r^2$, we keep $\omega_d\Phi$ terms but drop ω_d terms involving the fluid moments, yielding:

$$\frac{\partial}{\partial t}\delta p = -B\nabla_\parallel \frac{q_\parallel}{B} + B^4 \nabla_\parallel \frac{q_\perp}{B^4} - 2\nabla_\parallel u_\parallel - u_\parallel \nabla_\parallel \ln B - i\omega_d \Phi - \nu_{ii}\delta p. \tag{5.33}$$

At this point it is convenient, but not necessary, to assume that the flows are incompressible. Incompressibility is enforced by setting $\partial n/\partial t = 0$ in Eq. (5.25), which forces the divergence of parallel flow to balance the divergence of $\mathbf{E} \times \mathbf{B}$ flow, $\nabla \cdot \mathbf{v}_E = 2i\omega_d\Phi$:

$$B\nabla_\parallel \frac{u_\parallel}{B} = -2i\omega_d\Phi. \tag{5.34}$$

This removes the fast parallel sound wave time scale and simplifies the analysis. Using incompressibility in Eq. (5.33), some of the $u_\parallel$ and $\omega_d\Phi$ terms cancel. The remaining $u_\parallel$ and $\omega_d\Phi$ terms can be written in terms of the poloidal flow using $v_\theta = u_\parallel \epsilon b_z/q + ik_r h b_z \Phi$, from Eq. (5.21). The evolution of δp is then given by:

$$\frac{\partial}{\partial t}\delta p = -B\nabla_\parallel \frac{q_\parallel}{B} + B^4 \nabla_\parallel \frac{q_\perp}{B^4} - 3v_\theta \frac{\epsilon_n \sin\theta}{h} - \nu_{ii}\delta p, \tag{5.35}$$

Thus δp is driven by poloidal flow and damped by ion-ion collisions and parallel heat flows. Collisions relax the distribution function toward a Maxwellian, which causes isotropization of $T_\parallel$ and $T_\perp$, damping δp. The physical mechanism by which poloidal flow drives δp is a bit more subtle. Consider a poloidal flow which brings plasma from the outer midplane to the inner midplane, where B is larger. Because $\mu = v_\perp^2/2B$ is conserved, as B increases, $T_\perp$ increases. Similarly, from conservation of canonical toroidal angular momentum, $T_\parallel$ decreases, so poloidal flow drives a difference between $p_\parallel$ and $p_\perp$. This δp in turn damps the parallel flow, as shown by

Eq. (5.32). Since the toroidal flow is constant, this parallel flow damping leads to poloidal flow damping, as follows. Again using incompressibility, hv_θ is independent of θ. Then with some manipulation, $u_\parallel/h$ can be written in terms of $\langle hv_\theta\rangle$ and $\langle hv_\phi\rangle$:

$$\frac{u_\parallel}{h} = \frac{q}{\epsilon b_z}\left(\left\langle\frac{1}{h^2}\right\rangle - \frac{b_z^2}{\langle h^2\rangle}\right)\langle hv_\theta\rangle + \frac{b_z}{\langle h^2\rangle}\langle hv_\phi\rangle . \tag{5.36}$$

Evaluating the flux surface averages to lowest order in ϵ, $\langle h^2\rangle \approx 1+\frac{3}{2}\epsilon^2$ and $\langle 1/h^2\rangle \approx 1+\frac{1}{2}\epsilon^2$, leads to:

$$\frac{u_\parallel}{h} = (1+2q^2)\frac{\epsilon}{q}\langle hv_\theta\rangle + \langle hv_\phi\rangle . \tag{5.37}$$

Since the toroidal flow is constant, $\partial\langle hv_\phi\rangle/\partial t \approx 0$, Eq. (5.32) becomes:

$$\frac{\partial}{\partial t}\left\langle\frac{u_\parallel}{h}\right\rangle = (1+2q^2)\frac{\epsilon}{q}\frac{\partial}{\partial t}\langle hv_\theta\rangle = \frac{1}{2\pi}\int d\theta\frac{b_z\epsilon_n\epsilon\sin\theta}{qh}(p_\parallel - p_\perp). \tag{5.38}$$

In the Pfirsch-Schlüter regime (easiest, but least relevant to present day experiments), collisions keep $q_\parallel$ and $q_\perp$ small. Considering slow evolution compared to the sound wave time scale, we can look at the average evolution of δp by ignoring $\partial\delta p/\partial t$. Then δp in Eq. (5.35) is determined by the balance between the drive from the poloidal flow and the damping from collisional isotropization:

$$\delta p = -3v_\theta\frac{\epsilon_n\sin\theta}{\nu_{ii}h}. \tag{5.39}$$

Plugging this into Eq. (5.38), using the fact that hv_θ is independent of θ, and integrating over θ to lowest order in ϵ yields:

$$(1+2q^2)\frac{\epsilon}{q}h\frac{\partial v_\theta}{\partial t} = -3hv_\theta\left\langle\frac{b_z\epsilon_n^2\epsilon\sin^2\theta}{q\nu_{ii}h^4}\right\rangle, \tag{5.40}$$

The flux surface average on the right hand side can now be evaluated, which to lowest order in ϵ gives a poloidal damping rate of:

$$\gamma = -\frac{3}{2}\frac{\epsilon_n^2}{(1+2q^2)\nu_{ii}}. \tag{5.41}$$

Here both γ and ν_{ii} have been normalized to v_{ti}/L_n. In dimensional form, this is:

$$\gamma = -\frac{3}{2}\frac{v_{ti}^2}{(1+2q^2)\nu_{ii}R^2} = -\frac{3}{2}\frac{\omega_{ti}^2}{(2+1/q^2)\nu_{ii}}, \tag{5.42}$$

where $\omega_{ti} = v_{ti}/qR$. This expression matches the Pfirsch-Schlüter result of [Hassam and Kulsrud, 1978] exactly.

Now consider the less collisional plateau and banana regimes. Here the ν_{ii} term in Eq. (5.35) is negligible, and the dominant balance is between the heat flux terms, which damp δp, and poloidal flow, which drives δp. In these "collisionless" regimes, the heat fluxes primarily come from the Landau damping terms in the gyrofluid equations. For low frequencies, Eq. (2.95) and (2.96) reduce to $\sqrt{2}D_\parallel|k_\parallel|q_\parallel \approx -(3+\beta_\parallel)\nabla_\parallel T_\parallel$ and $\sqrt{2}D_\perp|k_\parallel|q_\perp \approx -\nabla_\parallel T_\perp$. Using $k_\parallel \approx 1/qR$ (in our dimensionless units, $k_\parallel$ is normalized to L_n, so $k_\parallel \approx \epsilon_n/q$), this approximately leads to:

$$\delta p \approx -3\sqrt{\frac{\pi}{2}}\frac{v_\theta q \sin\theta}{h} \tag{5.43}$$

Plugging this into Eq. (5.38) gives:

$$(1+2q^2)\frac{\epsilon}{q}h\frac{\partial v_\theta}{\partial t} = -3\sqrt{\frac{\pi}{2}}hv_\theta\left\langle\frac{b_z\epsilon_n\epsilon\sin^2\theta}{h^4}\right\rangle. \tag{5.44}$$

Evaluating the flux surface average to lowest order in ϵ yields the collisionless poloidal flow damping rate from the toroidal gyrofluid equations:

$$\gamma = -\frac{3}{2}\sqrt{\frac{\pi}{2}}\frac{q\epsilon_n}{1+2q^2}, \tag{5.45}$$

which in dimensional form is:

$$\gamma = -\frac{3}{2}\sqrt{\frac{\pi}{2}}\frac{\omega_{ti}}{(2+1/q^2)}. \tag{5.46}$$

This matches the plateau results of [Hirshman, 1978] and [Stringer, 1973] within a factor of 1.5, and also agrees with [Stix, 1973] if $(1+2q^2)$ is replaced by 1, since he was working in slab geometry, with modulated B.

In the banana regime, the neoclassical calculation of the poloidal flow damping rate is not as straightforward as in the plateau regime. Using the static values for the parallel viscosity coefficients, [Hirshman, 1978] found:

$$\gamma = -\frac{q^2\nu_{ii}}{1.29\epsilon^{3/2}(1+2q^2)}, \tag{5.47}$$

which is the same expression in dimensional and dimensionless form. This large damping rate violates the assumption $\omega \ll \nu_{ii}$ which calls the use of the static viscosity coefficients into question; a point which [HIRSHMAN, 1978] emphasized. Earlier works found $\gamma \propto -\nu_{ii}/\epsilon$ [STIX, 1973] and $\gamma \propto -\nu_{ii}$ [ROSENBLUTH *et al.*, 1971]. Later neoclassical expressions for the poloidal flow damping rate were derived without using the static parallel viscosity coefficients and found $\gamma \propto -\nu_{ii}$ [SHAING and HIRSHMAN, 1989], $\gamma \propto -\nu_{ii}/\epsilon^{1/2}$ [TAGUCHI, 1991], and $\gamma \propto -\nu_{ii}/\epsilon$ [HSU *et al.*, 1994]. Since ϵ is small, these results are extremely different. These last three works, instead of using the static parallel viscosity coefficients, solve for the time dependent distribution function, f_i. However, when solving for f_i they order $\partial f_i/\partial t \sim C(f_i) \ll \omega_{ti} f_i$, so these calculations miss any collisionless damping processes which occur on a faster time scale. As [STIX, 1973] argued, collisionless transit-time magnetic pumping dominates for short time scales, $t < \omega_{bi}^{-1}$. The analytic damping rate calculated from the toroidal gyrofluid equations in the banana and plateau regimes, Eq. (5.45), is consistent with this. Dimits' interpretation of poloidal flow damping in collisionless gyrokinetic particle simulations is also based on Stix's transit-time magnetic pumping picture [DIMITS, 1994]. The gyrofluid damping rates are compared to the neoclassical results of [HIRSHMAN, 1978] in Fig. 5.9. The results agree in the plateau and Pfirsch-Schlüter regimes. In the banana regime, transit-time magnetic pumping dominates for times $t \lesssim \omega_{ti}^{-1}, \omega_{bi}^{-1}$, and at later times the damping is governed by collisional processes.

The analytic gyrofluid results for the flow damping rates in Eqs. (5.41) and (5.45) are now compared with numerical solutions of the full toroidal gyrofluid equations without making any of the approximations used above. A flow with both toroidal and poloidal components is initially imposed and is linearly evolved in time. The parameters used are $k_r\rho_{i0} = 0.01$, $\epsilon = 0.1$ and $q = \epsilon_n = 1$; the scaling of Eqs. (5.41) and (5.45) with q and ϵ_n have also been checked, but are not shown here. Fig. 5.10 and 5.11 show the linear damping of these flows for the Pfirsch-Schlüter, plateau, and banana regimes. Here incompressibility is not enforced, so there are oscillations during the damping of the flow; it is not a purely exponential decay. The analytic gyrofluid expressions above compare favorably with the full numerical solutions. In the plateau and banana regimes, after an initial rapid damping phase, a finite poloidal flow is maintained which is damped on a slower collisional time scale. In contrast to the neoclassical banana regime results (valid only for longer time scales), no significant differences are seen between the plateau and banana damping rates in this initial strong damping phase.

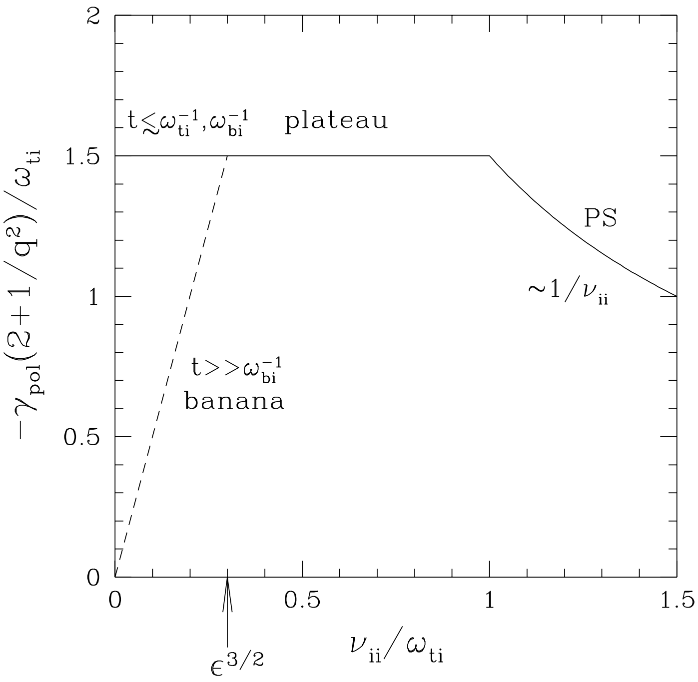

Figure 5.9: Poloidal flow damping rates in various collisional regimes. The gyrofluid results (solid) match the neoclassical results in the Pfirsch-Schlüter and plateau regimes. For short time scales ($t \lesssim \omega_{ti}^{-1}, \omega_{bi}^{-1}$), transit-time magnetic pumping dominates in the banana regime. The neoclassical result of [Hirshman, 1978] (using static parallel viscosity coefficients) is also shown in the banana regime (dashed). Because the neoclassical calculations assume that the distribution function evolves on a collisional time scale, they miss the rapid collisionless damping, and are only valid for $t \gg \omega_{bi}^{-1}$.

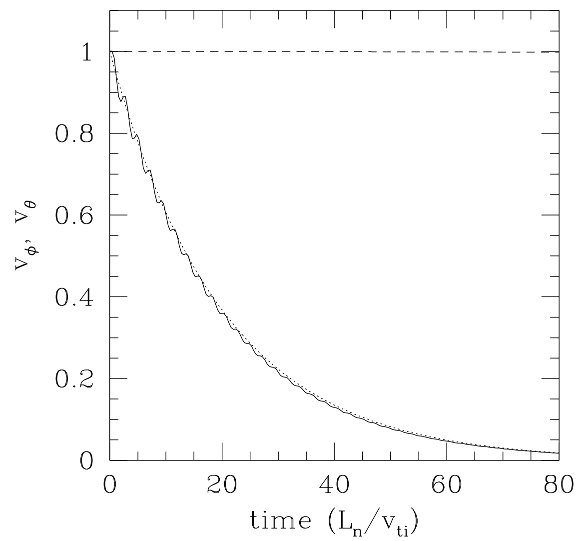

Figure 5.10: Poloidal flow damping in the Pfirsch-Schlüter regime, $\nu_{ii}/\omega_{ti} = 10.0$. The poloidal flow (solid) from simulations agrees with the analytic result Eq. (5.41) (dotted). The toroidal flow (dashed) is constant, demonstrating that toroidal angular momentum is well conserved.

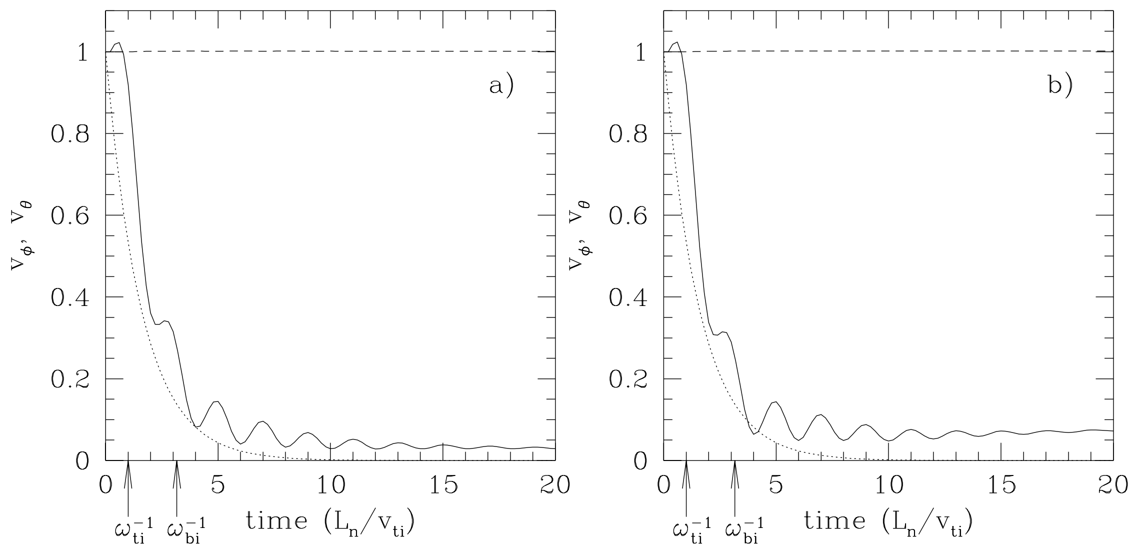

Figure 5.11: Poloidal flow damping in (a) the plateau regime, $\nu_{ii}/\omega_{ti} = 0.1$, and (b) the banana regime, $\nu_{ii}/\omega_{ti} = 0.001$. The poloidal flow (solid) from simulations agrees with the analytic gyrofluid result Eq. (5.45), and the toroidal flow (dashed) is again well conserved. Transit-time magnetic pumping dominates for short time scales $t \lesssim \omega_{ti}^{-1}\omega_{bi}^{-1}$, and at later times the damping is governed by collisional processes.

For the short time scales of the turbulence, transit-time magnetic pumping is the dominant poloidal flow damping process in the banana and plateau regimes. The small scale $\mathbf{E} \times \mathbf{B}$ flows are randomly generated by the turbulence, and damped according to Eq. (5.45). A bounce time later, when Eq. (5.45) is no longer valid, the turbulence has evolved into a different state, generating new flows. Because the turbulence is quite sensitive to balance between the nonlinear generation and the linear damping of the poloidal flow, it is important that the gyrofluid equations accurately model this process. Things get slightly more complicated for $k_r \rho_i \sim \mathcal{O}(1)$, and it is more difficult to check our models in this regime. Future work is needed to fully resolve this issue, but it appears that the toroidal gyrofluid equations are accurately modeling this process.

5.4 Nonlinear Simulation Results with Trapped Electrons

Although the adiabatic electron assumption may lead to a reasonable description of ITG driven turbulence in some regimes (e.g., when the electrons are very collisional so trapped electrons are wiped out, but not so collisional that the parallel dynamics are affected), in general, nonadiabatic electron effects should be taken into account. It is conceivable that if $\chi_i \gg \chi_e, D$, the electrons could be passively advected by toroidal ITG driven turbulence with little effect on the ion transport, but in general $\chi_i \sim \chi_e \sim D$. Clearly when $\chi_e > \chi_i$, nonadiabatic electron effects will be important. Further, electrons are typically in the banana regime ($\nu_{*e} < 1$), except in the collisional extreme edge and in the extreme core where the trapped fraction $\sqrt{\epsilon}$ is small, indicating that collisions are usually not large enough to completely wipe out the nonadiabatic electron response. Again, $D, \chi_e \neq 0$ guarantees that the electrons are significantly nonadiabatic.

In this section, the effects of nonadiabatic electrons are investigated with nonlinear simulations. These results should be considered preliminary. The effect of electron collisionality on the predicted transport is shown in Fig. 5.12 for the parameters $\eta_i = \eta_e = 3$, $q = 1.5$, $\hat{s} = 1$, $\epsilon_n = 1/3$, $\epsilon = 1/6$ and $T_i = T_e$, corresponding to the linear results in Fig. 3.5. For high collisionality, $\nu_{\text{eff}} L_n / v_{ti} = 10$ ($\nu_{*e} = 2$), the electron response is nearly adiabatic. The ion thermal flux, $\chi_i \approx 4\rho_i^2 v_{ti}/L_n$,

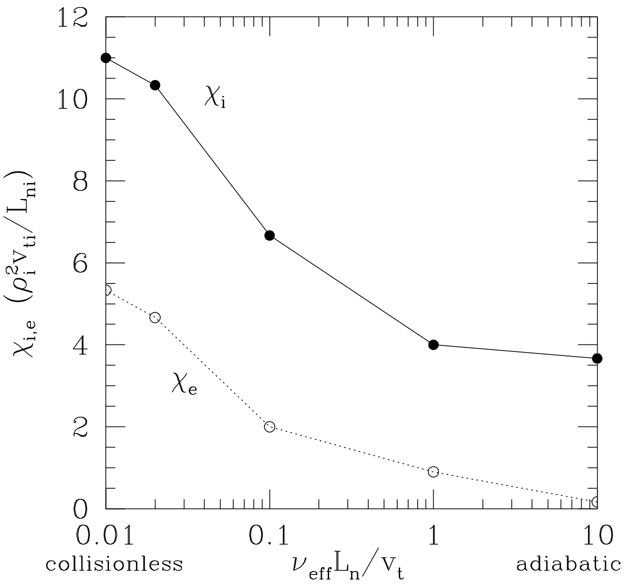

Figure 5.12: Fully nonlinear simulation results with trapped electrons, varying electron collisionality, for ITG driven turbulence at $\eta_i = \eta_e = 3$. As ν_{*e} is reduced, the electrons become destabilizing, until $\chi_i \sim 3\chi_i^{\text{adiabatic}}$ in the collisionless limit.

is the same as obtained with adiabatic electrons and χ_e is very small. As ν_{eff} is reduced, the electrons become destabilizing. In the collisionless limit, $\nu_{*e} = 0.002$, $\chi_i \approx 11\rho_i^2 v_{ti}/L_n$ and $\chi_e \approx 5\rho_i^2 v_{ti}/L_n$. Although for these parameters the turbulence is driven by toroidal ITG modes ($\eta_i = 3$, $L_{Ti}/R = 0.1$), electrons increase χ_i by up to a factor of three over simulations with adiabatic electrons.

Fig. 5.13 shows results from another set of nonlinear simulations showing the effect of ∇T_i. Beginning with the reference case $\eta_i = \eta_e = 3$, $q = 1.5$, $\hat{s} = 1$, $\epsilon_n = 1/3$, $\epsilon = 1/6$, $T_i = T_e$, and $\nu_{*e} = 0.02$, ∇T_i is reduced by lowering η_i holding $L_{ne} = L_{ni}$ and L_{Te} fixed. These nonlinear runs correspond to the linear results in Fig. 3.6. If the electrons are adiabatic, when η_i is reduced below the adiabatic η_i^{crit}, the plasma is stable and the turbulent flux vanishes (solid squares in Fig. 5.13). With trapped electrons at low electron collisionality, below the adiabatic η_i^{crit} the turbulence is driven by unstable trapped electron modes. The ion heat flux $Q_i = \langle v_{Er} p_i \rangle$ drops below Q_e for $\eta_i < \eta_i^{\text{crit}}$, consistent with the quasilinear ratios where $Q_i > Q_e$ for the toroidal ITG mode and $Q_i < Q_e$ for the TEM [Rewoldt

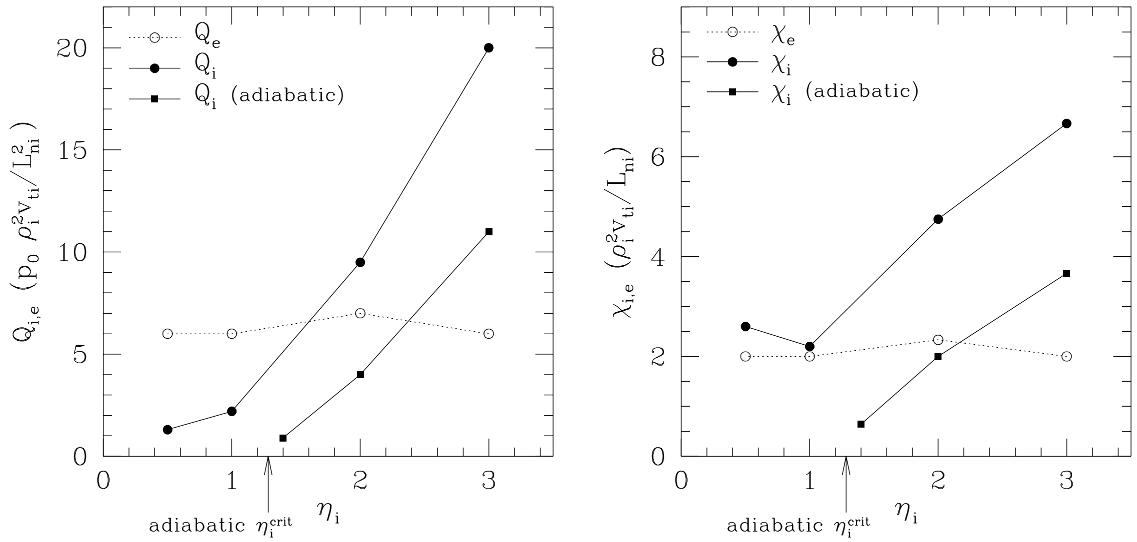

Figure 5.13: Nonlinear simulations predict χ_i/χ_e in experimental range even for $\eta_i < \eta_i^{\rm crit}$ adiabatic at low electron collisionality. At $\nu_{*e} = 0.02$, as η_i is reduced holding $\eta_e = 3$ fixed, Q_i drops below Q_e as the ITG mode evolves into TEM, but since ∇T_i is getting weaker, χ_i stays above or comparable to χ_e. Lowering η_e reduces χ_i and χ_e (weaker TEM drive).

and Tang, 1990]. However, since $Q = \chi \nabla T$, because ∇T_i is decreasing, χ_i stays above or comparable to χ_e. The relative magnitudes of χ_i and χ_e are within the experimental range, where typically $\chi_i \sim \chi_e$. The parameters of this scan were specifically chosen to investigate strongly driven TEM turbulence at $\eta_i < \eta_i^{\rm crit}$. A physically more realistic scan would not hold $\eta_e = 3$ fixed; $\eta_e = \eta_i$ is more likely. When the scan is repeated decreasing both η_e and η_i simultaneously, both χ_i and χ_e are reduced in the TEM regime, by roughly a factor of three.

These nonlinear results show that the most striking effect of trapped electrons is to soften the $\eta_i^{\rm crit}$ or $L_{Ti}^{\rm crit}/R$ threshold which exists with adiabatic electrons. When the turbulence is driven by trapped electron modes, below $\eta_i^{\rm crit}$, Q_i is reduced, so in this sense there is still a threshold for the ion heat transport, but it is not a sharp threshold at low collisionality. For the moderate ν_{*e} of many L-modes, there is marginal behavior, but at lower ν_{*e} there may still be a fairly strong TEM drive with less marginal features. Mapping out precisely when this happens is now possible with our simulations with trapped electrons. As shown above, the TEM drive can strongly affect both ion and electron transport. It is thus expected that both χ_i and χ_e will depend on electron collisionality and *electron* density and temperature gradients in low collisionality regimes, particularly when η_i is low and the TEM dominates.